m -Phenylenediammonium as a New Spacer for Dion–Jacobson Two-Dimensional Perovskites

Lili Gao, Xiaotong Li, Boubacar Traore, Yalan Zhang, Junjie Fang, Yu Han, Jacky Even, Claudine Katan, Kui Zhao, Shengzhong Liu, et al.

m-Phenylenediammonium as a New Spacer for Dion−Jacobson 2D Perovskites

Lili Gao,[a,b†] Xiaotong Li,[b†] Boubacar Traoré,[d] Yalan Zhang,[a] Junjie Fang,[a] Yu Han,[a] Jacky Even,[c] Claudine Katan,[d] Kui Zhao,[a] Shengzhong (Frank) Liu, *[a, e, f] and Mercouri G. Kanatzidis,*[b]

[a]*Key Laboratory of Applied Surface and Colloid Chemistry, Ministry of Education; Shaanxi Key Laboratory for Advanced Energy Devices; Shaanxi Engineering Lab for Advanced Energy Technology; Institute for Advanced Energy Materials; School of Materials Science and Engineering, Shaanxi Normal University, Xi'an 710119, China.*

[b]*Department of Chemistry, Northwestern University, Evanston, Illinois 60208, United States.*

[c] *Univ Rennes, INSA Rennes, CNRS, Institut FOTON, UMR 6082, Rennes F-35000, France*

[d]*Univ Rennes, ENSCR, INSA Rennes, CNRS, ISCR (Institut des Sciences Chimiques de Rennes), UMR 6226, Rennes F-35000, France*

[e]*Dalian National Laboratory for Clean Energy; iChEM, Dalian Institute of Chemical Physics, Chinese Academy of Sciences, Dalian 116023, China.*

[f]*University of the Chinese Academy of Sciences, Beijing 100039, China.*

ABSTRACT:

Two-dimensional (2D) halide perovskites come in several distinct structural classes and exhibit great tunability, stability and high potential for photovoltaic applications. Here, we report a new series of hybrid 2D perovskites in the Dion−Jacobson (DJ) class based on aromatic m-Phenylenediammonium (mPDA) dications. The crystal structures of the DJ perovskite materials (mPDA)$MA_{n-1}Pb_nI_{3n+1}$ (n = 1, 2, 3) were solved and refined using single crystal X-ray crystallography. The results indicate a short I···I interlayer distance of ~4.00 − 4.04 Å for the (mPDA)$MA_{n-1}Pb_nI_{3n+1}$ (n = 2 and 3) structures, which is the shortest among DJ perovskites. However, Pb−I−Pb angles are as small as ~158-160º reflecting large distortion of the inorganic framework that results in larger band gaps for these materials compared to other DJ analogues. Density functional theory calculations suggest appreciable dispersion in the stacking direction, unlike the band structures of the Ruddlesden-Popper (RP) phases which exhibit flat bands along the stacking direction. This is a consequence of a short interlayer I···I distances that can lead to inter-layer electronic coupling across the layers. The solution deposited films (nominal (mPDA)$MA_{n-1}Pb_nI_{3n+1}$ compositions of n = 1−6) reveal improved surface coverage with increasing nominal n value with the higher-n films being composed of a mixture of n=1 and bulk 3D $MAPbI_3$ perovskites. The films made from solutions of these materials behave differently from those of other 2D iodide perovskites and their solar cells have a mixture of n=1 DJ and $MAPbI_3$ as the light absorbing semiconductors.

Introduction

Halide perovskites are impacting several optoelectronic based technologies such as solar cells,[1-5] detectors,[6-10] light-emitting diodes,[11-15] because of their outstanding properties, including high absorption coefficient,[16] tunable exciton binding energy (low exciton binding energy for 3D perovskites at RT or tunable exciton binding energies in low-dimensional perovskites),[17] long-range charge transport,[18] low trap density,[19] high defect tolerance[20] and low-cost solution processability.[21] The record efficiency for the perovskite solar cells currently stands at > 25%.[22] The most common three-dimensional (3D) perovskites adopt a general formula of AMX_3 (A = methylammonium (MA, $CH_3NH_3^+$), formamidinium (FA, $CH_3(NH_2)_2^+$), or Cs^+; M = Sn^{2+} or Pb^{2+}; X = Cl^-, Br^-, or I^-). The inorganic ions form the octahedral frame with $[MX_6]^{4-}$, and the small organic cations occupy cuboctahedral voids within the structure and counterbalance the charge of the $[MX_6]^{4-}$ extended anion.[23]

When large spacer cations are inserted into the 3D structure along different directions, such as (100), (110) and (111) planes, 2D perovskites can be obtained.[23, 24] These perovskites have impressive structural diversity and great potential in optoelectronic applications.[25-27] The (100)-oriented 2D perovskites are the most common ones, which can be further categorized into the Ruddlesden−Popper (RP) phases,[28] the Dion−Jacobson (DJ) phases,[29] and the alternating cation in the interlayer space (ACI) phases,[30] with the general formulas of $A'_2A_{n-1}M_nX_{3n+1}$, $A''A_{n-1}M_nX_{3n+1}$, and $A'A_nM_nX_{3n+1}$, respectively. The A' is monovalent (+1) and A'' is divalent (+2) large cations, which can intercalate into the anionic sheets of the 2D perovskites. The layer-

number n not only enriches the structural complexity of the perovskite family but also allows for the fine-tuning of the optoelectronic properties as they offer tunable natural quantum wells.[17, 31-35]

The RP phases incorporate monovalent spacer cations interdigitating between the layers, and the inorganic layers are usually staggered. In contrast, the DJ phases incorporate short divalent cations and the inorganic layers have the tendency to stack exactly on top of each other. For linear diammonium cations $NH_3(CH_2)_mNH_3^{2+}$,[36, 37] even when the carbon-chain length is as short as m = 4, the adjacent inorganic layers are still slightly offset because of strong hydrogen-bonding of the cation. For shorter diammonium cation $(CH_3)_3NCH_2CH_2NH_3^{2+}$, it can form the DJ phase $((CH_3)_3NCH_2CH_2NH_3)SnI_4$ even though it is asymmetric.[38] When more compact cyclic diammonium cations, such as x- (aminomethyl)piperidinium (AMP, x = 3 and 4), are incorporated, multilayer DJ phases can form with eclipsed octahedra. The aromatic analogues, x-(aminomethyl)pyridinium (AMPY, x = 3 and 4), can also template the DJ phases.[39] When both amino groups are primary amines, such as 1,4-phenylenedimethanammonium, the DJ phase can also form in principle.[40] However, a conclusive structural determination is lacking partly because of the low solubility of the cation in HI. A similar cation with amino groups directly attached to the phenyl ring, p-phenylenediammonium, forms 1D structure with edge-sharing octahedra,[41] which suggests symmetric diammonium cations cannot guarantee the formation of the DJ phase, while asymmetric cations may also be able to form the DJ phase. However, the

meta analogue, mPDA, does form the n = 1 2D structure for chloride perovskite.[42] It offers the opportunity to further expand the family of DJ layered perovskites. The eclipsed stacking and short distance between the layers are also beneficial for the charge transport in photovoltaic devices. The field of the 2D perovskite solar cells with DJ phases has developed rapidly since we reported the first multilayer DJ structures, [29, 43, 44] however, the determination of the single-crystal structures is lagging behind,[45] therefore detailled crystallographic studies are nowadays priority to expand the DJ family and bring it on the same footing as the RP one. Here, we report a new series of DJ phases with mPDA, forming (mPDA)$(MA)_{n-1}Pb_nI_{3n+1}$ (n = 1, 2, 3) 2D perovskites. Detailed crystallographic investigations show that the inorganic layers stack exactly on top of each other. These materials exhibit smaller average Pb−I−Pb angles than other 2D perovskites using 3AMP, 4AMP and BA. The distorted inorganic framework in turn gives rise to a relatively larger band gap. DFT calculations suggest noticeable band dispersion in the stacking direction because of the small interlayer distance. The optical properties and morphology of (mPDA)$(MA)_{n-1}Pb_nI_{3n+1}$ (n = 1-6, nominal composition) perovskite films are suitable for use in solar cell devices but the film formation behavior is different from that of currently known 2D perovskite iodides.

Results and Discussions

Single crystal growth

Single crystals of (mPDA)$(MA)_{n-1}Pb_nI_{3n+1}$ (n = 1, 2, 3) were grown using a step-cooling method as reported previously to avoid the precipitation of non-perovskite light-yellow

phase.[46-48] In this method, after everything is dissolved in the solution under heating to a boil, the solution temperature is first lowered to 120°C, which is right below the boiling point of HI (127°C), so that only the desired 2D perovskite phases can grow. Suitable stoichiometric ratios of PbO and MACl, and sub-stoichiometric ratio of mPDA were dissolved in HI solution for the desired layer-number (n = 2 and 3). For n=1, it is difficult to obtain high quality single crystals directly from HI solution because of the low solubility. Instead, we found that n = 1 chloride perovskite can be easily grown from HCl as (mPDA)$PbCl_4$ and then be redissolved in HI[42] giving high quality (mPDA)PbI_4 crystals. The color of the crystals varies from orange (n = 1) to red (n = 2) to dark red (n = 3), as shown in Figure S1.

The precise crystal structures of (mPDA)$MA_{n-1}Pb_nI_{3n+1}$ (n = 1, 2, 3), shown in **Figure 1**, were determined using single-crystal X-ray diffraction. Selected crystallographic data and structural refinements for all compounds reported here are listed in **Table 1**, with more detailed crystallographic data provided in the **Tables 2-3**. The compounds were refined in the noncentrosymmetric monoclinic space group (*Cc*) for n=1 and 2, and noncentrosymmetric orthorhombic space group ($Pmc2_1$) for n = 3. The successful synthesis of the desired n member was further confirmed by powder X-ray diffraction (PXRD), as shown in **Figure 2a,** and the number of the low-angle peaks below 2θ = 14° is consistent with the expected layer-number. The characteristic diffraction peaks for n = 1, 2, and 3 crystals match well with calculated PXRD, as shown in **Figure 2b-d**.

The n = 1 structure is highly distorted (Figure 1a) and the inorganic layers ar slightly offset, with a layer shift factor of (0.11, 0.12). In an ideal cubic structure, the four adjacent Pb atoms in a plane form a square. In lower symmetry (tetragonal or orthorhombic) structures, two opposite edges of the square are "pulled-in" and the other two are "pushed-out". From the top view, we can see rhombus-shaped voids, such as in the structures of n = 2 and 3 (Figure 1b, c). However, for the n = 1 structure, two adjacent edges are "pushed-out" and the other two are "pulled-in", so from the top view, trapezoid-shaped voids are observed. The Pb atoms are off-centered in the octahedra and the I-Pb-I angle deviate significantly from 90°. The deformation of octahedra can also be seen from the values of bond angle variance (σ) calculated by the expression, $\sigma^2 = \sum_{i=1}^{12} (\theta_i - 90)^2/11$, where θ_i is the individual I-Pb-I bond angle. The bond angle variance values for n = 1, 2 and 3 structures are 234.2, 1.1 and 3.0, respectively. The large σ value for the n = 1 phase originates from the significant deviation of the Pb-I-Pb angles from 90°. This is probably because the aromatic dication spacer is very short and rigid, all the atoms must stay on the same plane except for the Hs on the amino groups that can rotate. It has been reported that some cations cannot form n = 1 perovskite by itself because the size is too small to template the 2D structure, but they can form more proper multilayer 2D perovskites with MA inside the cage.[49] We can calculate the lattice mismatch by the difference of the adjacent Pb-Pb distance of the 2D structures with that of the standard $MAPbI_3$.[50] By comparison to other DJ and RP phases, mPDA (n=1) has both the largest mismatch with 3D $MAPbI_3$ and largest in-plane anisotropy (Table 4), which caused large distortion and strain in the structure. By

contrast, in the multilayer structures some of this strain can be relieved to an extent because of the templating effect of the A-site cation MA. The n = 1 phase has a much smaller adjacent Pb···Pb distance than the 3D $MAPbI_3$. When the MA cation is added to the cage to form the multilayer phases, it will expand the cage the adjacent Pb···Pb distance also increases, so the lattice mismatch between the inorganic and organic layers decreases, which helps to relieve the strain. But the trend remains that the mPDA compounds exhibit the largest lattice mismatch. The anisotropy of the structure, calculated by $[Pb_1{-}Pb_3 - Pb_1{-}Pb_5] /[(Pb_1{-}Pb_3 + Pb_1{-}Pb_5)/2]$, is also shown in Table 4. The mPDA compounds exhibit a larger anisotropy compared to the others, which originates from the irregular tilting of the Pb-I-Pb bonds (discussed above). All structures become more isotropic with increasing number of layers, as they become more like 3D $MAPbI_3$. The adjacent organic spacer cations adopt a tilted conformation in the n = 1 structure (Figure 1a).

For n = 2 and 3, the inorganic layers with corner-sharing octahedra stack exactly on top of each other, with layer shift factor of (0, 0),[51] so they belong to the DJ structural class. The octahedra are separated by the fully ordered mPDA cations. This is different from most aromatic spacer cations that are usually disordered,[52] and the cations need to be refined with restraints of bond lengths and bond angles. The mPDA rings are parallel to the stacking direction and adjacent cations adopt a face-to-edge configuration, which is also seen in the AMPY series.[26] As shown in **Figure 1d**, the amino groups are

pointing to the right and front, leading to a net dipole moment in the structure that results in the noncentrosymmetric space groups.

For 2D perovskites, the interlayer space between inorganic slabs plays a crucial role for electronic band structure of 2D materials and in turn for the out-of-plane charge transport. It has been shown that small interlayer distance can lead to a weak but notable electronic interaction across the interlayer and give rise to a small band dispersion in the stacking direction.[29, 53-55] The compact cation results in very short non-bonding I···I distance of 4.04 Å and 3.99 Å for n = 2 and 3 structures, respectively. This short I···I distance between the inorganic layers is expected to be beneficial for carrier transport. The penetration depth, defined by the distance between the amino group and the plane crossing the terminal iodine atoms, is 0.238 (0.349) Å, 0.404 (0.441) Å and 0.442 Å for the n = 1- 3 phases, respectively, which is smaller compared to other DJ phases such as $(xAMP)(MA)_{n-1}Pb_nI_{3n+1}$ and $(xAMPY)(MA)_{n-1}Pb_nI_{3n+1}$. This is because the primary amino group is connected to an alkyl linker and is free to rotate, but those of mPDA is rigid, which limits the penetration depth in the $(mPDA)(MA)_{n-1}Pb_nI_{3n+1}$ series.

Even though the octahedra in n = 2 and 3 structures are not as distorted as n = 1, they are still highly tilted, especially in the in-plane direction, which can be seen from the small Pb-I-Pb angles. The Pb-I-Pb angle can be further categorized into the equatorial angle which is parallel to the layer and the axial angle which is perpendicular to the inorganic layer. For n = 2 and 3 structures, the axial angles are close to 180°, while the equatorial angles deviate strongly from 180°. So, the average Pb-I-Pb angle is one of

the smallest among the reported structures of the same layer-number (**Figure 3**). It is an indication that the strain caused by lattice mismatch in the n=2 and 3 structures is not relaxed as efficiently as in other DJ phases (Table 4).

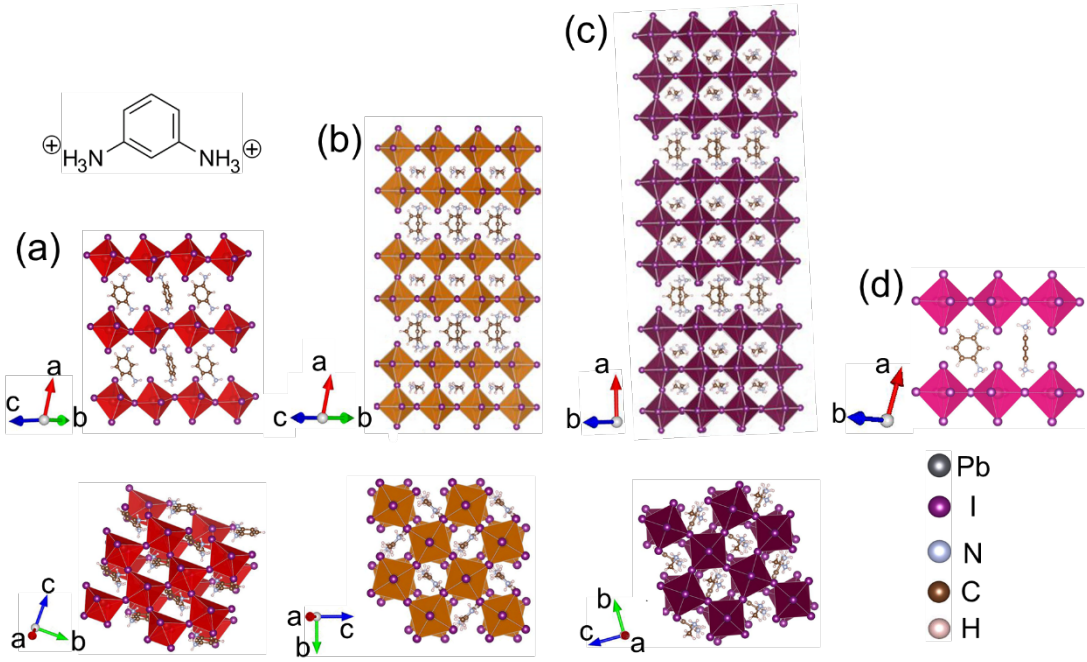

Figure 1. Crystal structures of (mPDA)$MA_{n-1}Pb_nI_{3n+1}$, (a) n = 1, (b) n=2 and (c) n=3, (d) the zoom of the spacer part in (c).

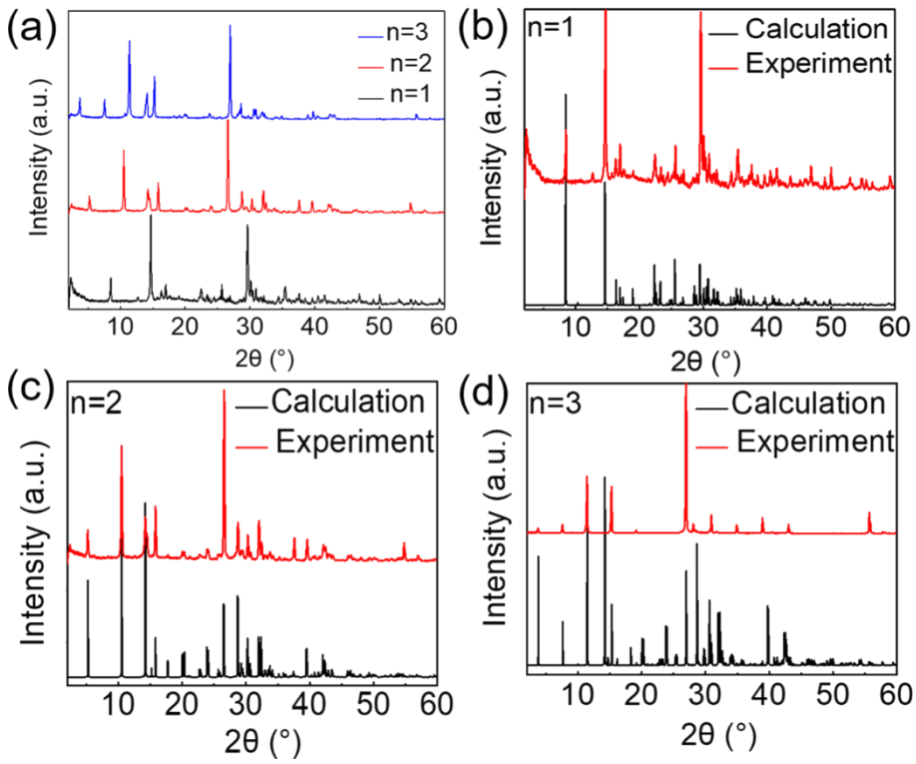

Figure 2. (a) Experimental PXRD patterns of (mPDA)$MA_{n-1}Pb_nI_{3n+1}$ (n=1, 2, 3) crystals. Calculated and experimental PXRD for the (mPDA)$MA_{n-1}Pb_nI_{3n+1}$, (b) n = 1, (c) n = 2, (d) n = 3.

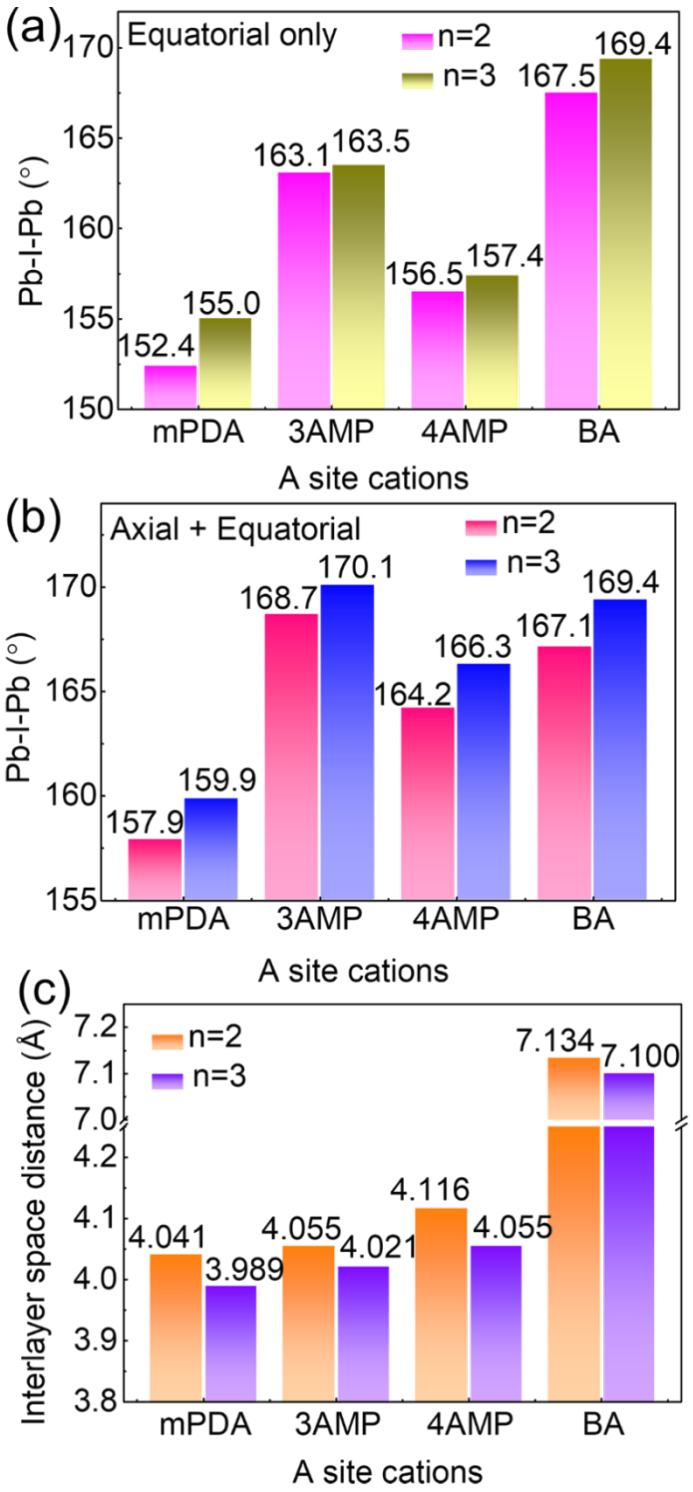

Figure 3. Comparison for (mPDA)$MA_{n-1}Pb_nI_{3n+1}$, (3AMP)$(MA)_{n-1}Pb_nI_{3n+1}$, (4AMP)$(MA)_{n-1}Pb_nI_{3n+1}$, and $(BA)_2(MA)_{n-1}Pb_nI_{3n+1}$, (n = 2 and 3), (a) average equatorial Pb-I-Pb angles, (b) average axial and equatorial Pb-I-Pb angles. (c) I···I interlayer distances.

Optical Properties and Electronic Structure Calculations

The absorption spectra of the (mPDA)$MA_{n-1}Pb_nI_{3n+1}$ (n = 1, 2, 3) exhibit high-energy absorption edges and low-energy exciton peaks (**Figure 4a**). In our previous works, we extracted the band gaps from the high-energy slope, which also matches the peak positions of the steady-state photoluminescence (PL) spectra. In the case of (mPDA)$MA_{n-1}Pb_nI_{3n+1}$ (n = 1, 2, 3), however, since the slope is not very sharp, we estimate the band gaps (E_g) from the PL emission peaks (**Figure 4b**). The bandgaps decrease with increasing layer thickness, from 2.42 eV, and 2.16 eV to 2.00 eV for the n = 1, 2, and 3 perovskites, respectively. The PL spectra were measured in a single point from the crystal surfaces, as indicated in the photographs shown in Figure S2.

Comparing the band gap and PL trend of this series with those of other reported 2D perovskites of the same layer-number, we find that the (mPDA)$(MA)Pb_2I_7$ compound shows higher band gap than $(BA)_2(MA)Pb_2I_7$ (BA = butylammonium) and (xAMP)$(MA)Pb_2I_7$ (x = 3 and 4), **Figure 4c**. For the n=3 set, the PL emission energy decreases as follows (mPDA)$(MA)_2Pb_3I_{10}$ ~ $(BA)_2(MA)_2Pb_3I_{10}$ > (4AMP)$(MA)_2Pb_3I_{10}$ > (3AMP)$(MA)_2Pb_3I_{10}$, **Figure 4d**. It is known that the Pb-I-Pb angles directly influence the band gap where smaller angles lead to less overlap of the Pb 6s and I 5p orbitals, resulting in higher bang gap.[56, 57] The average Pb-I-Pb angles for n = 2 and 3 phases follow the trend that mPDA < 4AMP < BA< 3AMP, as shown in **Figure 3a, b**. In the DJ phases, all the axial Pb-I-Pb angles are close to 180°, so the difference in the average Pb-I-Pb angles mainly comes from the equatorial ones (Table 2). For the n=3 compounds, the band gaps follow the trend mPDA = BA> 4AMP > 3AMP, while for

both the equatorial and average Pb-I-Pb angles the trend is mPDA < 4AMP < BA < 3AMP, which suggests that the Pb−I−Pb bond angle is not the only determinant factor.

Previously, we suggested that close interlayer distances via I···I interactions may result in slight widening of the bandwidth in the stacking direction, through a superlattice effect and concomitant small narrowing of band gap.[26, 30, 36] Across the DJ phases with mPDA, 3AMP and 4AMP, the closest I···I interlayer distance of ~ 4 Å is found with mPDA compared to the longest of ~ 7 Å for BA (see **Figure 3c**). The enhanced electronic interaction across the interlayer in DJ phases indeed counterbalances the effect of larger Pb-I-Pb angle distortions on the band gap.[29] For the DJ phases, all axial Pb-I-Pb angles are close to 180° and the equatorial angles present main deviations from 180°. All DJ phases exhibit smaller equatorial Pb-I-Pb angles than the RP phases (BA compound), but the 3AMP compounds still show the lowest band gap for both n = 2 and 3 thanks to sizeable superlattice effects related to short I···I interlayer distances.

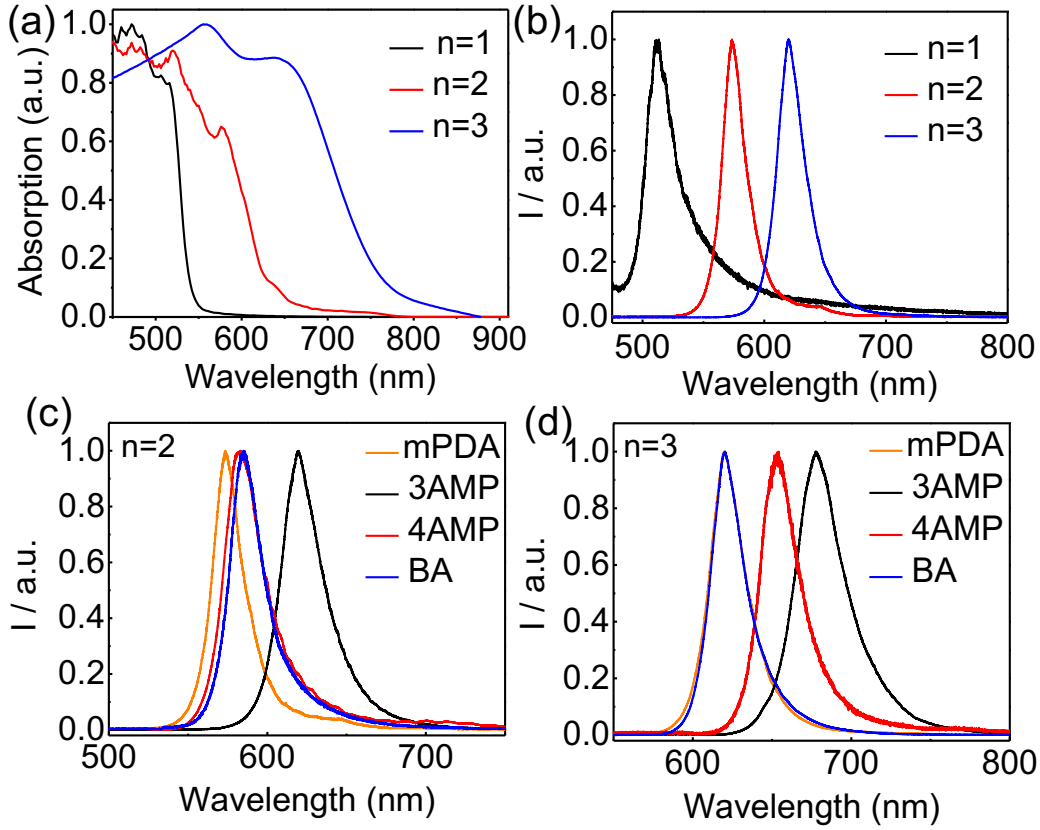

Figure 4. Optical properties of the (mPDA)$MA_{n-1}Pb_nI_{3n+1}$ (n=1, 2, 3) perovskites crystals. (a) Optical absorption spectra. (b) Steady state photoluminescence (PL) spectra. Comparison of the PL spectra for the (c) n = 2 and (d) n = 3 2D perovskites (mPDA)$MA_{n-1}Pb_nI_{3n+1}$, (3AMP)$(MA)_{n-1}Pb_nI_{3n+1}$, (4AMP)$(MA)_{n-1}Pb_nI_{3n+1}$, and $(BA)_2(MA)_{n-1}Pb_nI_{3n+1}$. (Note that the PL spectra of mPDA is bold so it can be seen when overlapping with BA)

Electronic Structure Calculations

The band structures of the n = 2 and 3 compounds were obtained from density functional theory (DFT) calculations using the experimental crystallographic structures. The Generalized Gradient Approximation (GGA) with revised-Perdew-Burke-Ernzerhof (revPBE) functional[58, 59] was used to describe the exchange-correlation term. Spin-orbit coupling (SOC) was included in its fully relativistic spin-DFT formalism.[60] Additional corrections of the band gaps, using the revisited Slater half-occupation

technique in the so-called DFT-1/2 implementation[61, 62], were performed and they generally exhibit a similar trend as with revPBE (Figure S3, Table S1). More computational details and results can be found in SI.

The band gaps of the DJ compounds are slightly indirect around the high-symmetry k points (Y, X or Z) due to slight Rashba spinor splitting as a result of the noncentrosymmetric nature of their space groups combined with the presence of giant spin-orbit coupling (Figure 5). The calculated band gaps for the mPDA n = 2 and n = 3 compounds are 0.92 eV and 0.86 eV, respectively, thus exhibiting a decreasing quantum confinement effect consistent with experimental results (Figure 4a, b). It is well known that DFT tends to underestimate the band gaps. Unlike the band structures of the Ruddlesden-Popper (RP) phases (Figure 5e), which exhibit flat bands in the stacking direction (Γ-Y), the band structures of the DJ phases show clear band dispersions along those directions in the Brillouin zone (Table 5). For instance, this can be seen in the mPDA compounds along Y-M_x and Γ-X directions of the Brillouin zone for n = 2 and 3, respectively (Figure 5a, b). This is related to the short interlayer distance, especially when the closest I···I distance is similar to the van der Waals radii, that can lead to inter-layer electronic coupling across the layers, with anti-bonding character at the high symmetry k-point.[39, 46] This should be beneficial to the charge transport along the stacking direction even though the charge mobility is still expected to be much larger in the in-plane direction (Table 5). The valence band maximum (VBM) mainly consists of the hybridization between I 5p-orbitals and Pb 6s-orbitals , while the conduction

band minimum (CBM) is dominated by the Pb 6p-orbitals with a little contribution of I 5p-orbitals (Figure S4), as expected from space group symmetries in 2D perovskites.[17] Since the I orbitals mainly contribute to the VBM, the close I···I distance leads to stronger band dispersion in the VBM than in the CBM. The band dispersion increases with increasing layer-number, as the materials becomes more 3D like. It is also worth noting that unlike other aromatic cations, the molecular orbitals of the organic spacer do not show up in the gap, which corresponds to a Type I quantum well structure in all cases. The calculated effective masses of the electrons and holes in the in-plane direction are shown in Table 5. The 3AMP compounds show the smallest effective masses, comparable to those of the BA compounds, which can be attributed to their large equatorial Pb-I-Pb angles close to 180°.

Comparing the band structures of (mPDA)(MA)Pb_2I_7 with those of (3AMP)(MA)Pb_2I_7 (4AMP)(MA)Pb_2I_7 and $(BA)_2$(MA)Pb_2I_7, we find that the DJ phases all show larger band dispersion than the RP phase in the stacking direction (Table 5). The calculated band gaps follow the experimental trend with E_g (mPDA) > E_g (4AMP) > E_g (3AMP). As discussed above, when the interlayer distances are similar, the Pb-I-Pb angle distortion is the main factor that can influence the band gap. Since the mPDA compound has the smallest Pb-I-Pb angle, followed by the 4AMP and then the 3AMP, the higher distortion level leads to less overlap between the Pb and I orbitals, thus higher band gap.

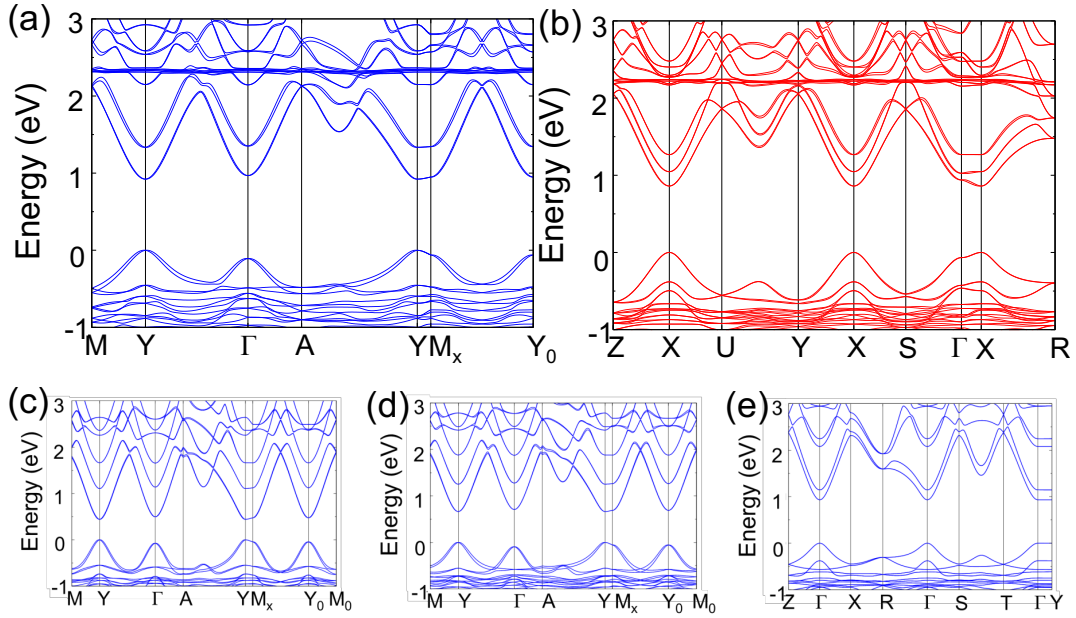

Figure 5. DFT calculations (with revPBE) of band structures for (mPDA)$MA_{n-1}Pb_nI_{3n+1}$ with n number of (a) n = 2, (b) n = 3, compared with the band structures of (c) (3AMP)$MAPb_2I_7$, (d) (4AMP)$MAPb_2I_7$ and (e) $(BA)_2MAPb_2I_7$.

Film properties and solar cell devices

Although single phase sample of the higher members of the series (mPDA)$MA_{n-1}Pb_nI_{3n+1}$ (n=4-6) were not prepared in this work, thin films aiming at various 2D perovskite compositions corresponding (mPDA)$MA_{n-1}Pb_nI_{3n+1}$ (n=1-6) were fabricated by dissolving stoichiometric ratios of the reactant precursors in N,N-Dimethylformamide (DMF). All the n values discussed in this part correspond to nominal or targeted values in thin films, but not necessarily to well defined layer-numbers as in n=2,3 pure 2D perovskite single crystals. The optical absorption edges of the resulting films shift rather quickly to higher wavelengths (**Figure 6a**). However, the absorption peak characteristic of the n = 1 phase at 493 nm is also observed for films of different nominal n numbers but its intensity is gradually decreased. This

indicates a co-existence of n=1 and 3D bulk phases in (mPDA)$MA_{n-1}Pb_nI_{3n+1}$ (n = 2-6) films because of a fast dynamical crystallization process. Moreover, our crystallographic study of n=2 and n=3 crystals shows that strain accumulation is not completely released for intermediate n values, as indicated by sizeable octahedral tilting and lattice mismatch compared to other 2D phases (Table 4). It is therefore not totally surprising that pure multilayered 2D phases are not favored in thin films.

The photoluminescence (PL) spectra of the films illuminated from the front side exhibit two peaks, as shown in **Figure 6b**. The n = 1 emission located at 512 nm decreases its intensity with increasing targeted n number of (mPDA)$MA_{n-1}Pb_nI_{3n+1}$ (n = 2-6) films, which is consistent with the decreased absorption intensity mentioned above and suggests decreased fraction of the n =1 phase. The second emission peak is around 773 nm, which is associated with the 3D bulk phase. These observations indicate that expected solution-casting of (mPDA)$MA_{n-1}Pb_nI_{3n+1}$ (n = 2-6) films tend to yield mixed phases of n = 1 and 3D. The change in the precursor solution only tune the ratio between those phases, but since there is no intermediate multilayer phases formed on the fim, the absorption and PL spectra do not shift with the nominal "n" value. This is also verified from XRD (**Figure 6c)**. The n = 1 phase can be observed for $n \leqslant 4$ films. While for n = 5 and 6 films, there is no distinct n = 1 diffraction peaks, which does not preclude the existence of n = 1 phase, instead it suggests sufficiently coherent crystallographic regions are not present in these films.

The SEM images of (mPDA)$MA_{n-1}Pb_nI_{3n+1}$ films indicate that the n = 1 film exhibits

poor coverage because of randomly stacked plate crystals of the n=1 phase with grain size of ~1-5 μm, **Figure S5**. Although the higher n films show improved surface coverage because the grain sizes of the n=1 phase which is present in them decrease to ~200-500-nm, we still observed severe phase separation with some long 2D plates randomly interspersed within small grains. The above results are consistent with the optical absorption spectroscopy observations that higher nominal n perovskite films tend to form a mixed phase of n = 1 2D and bulk 3D phases.

In addition, we investigated the light, heat, and humidity stability of (mPDA)$MA_{n-1}Pb_nI_{3n+1}$ (n = 1-6, nominal composition) films under the following conditions. The continuous light illumination test was conducted in air (temperature 22 ℃, humidity 35%) under standard 1 sun light intensity (AM 1.5G irradiation, 100 mW/cm^2). The long heating stability was conducted on a hot plate with temperature of 85 ℃, which placed in air (temperature 22 ℃, humidity 35%). The high humidity stability was conducted in a closed box with temperature of 22 ℃and humidity of 85%. All stability tests were done with as-fabricated films without any encapsulation. The results are shown in Figure S6, S7 and S8. The mixed films (n ≥ 2) exhibit considerable heating stability lasting for over 30 hours before thorough decomposition (Figure S6). For the light stability, films with n ≥ 2 kept black color until continuous illumination over 20 hours, film with n = 1 decomposed after 10 hours illumination (Figure S7). It is worth noting that the higher nominal n members do not exhibit the best stability performance. It is the middle members of n = 3 and 4 that exhibit the best stability. The films do not

exhibit great stability under high humidity of 85% (Figure S8), and some new phases form after 1 h. It is possible that the perovskite phase on the film interacts with the H_2O molecules and form a hydrate phase, since the 1,4PDA analogue is known to form the hydrates. This suggests a sealed in the device architecture or encapsulation, but a full undestaing and assessment of stability will requires considerably more optimization future exploration.

The PXRD and optical results discussed above (Figure 6a-c) suggest that dissolving the chemical precursors and then casting films of nominal n compositions does not give rise to the pure targeted 2D phases themselves but rather a combination of 2D n=1 phase and 3D $MAPbI_3$ in various fractions. Therefore, any solar cells prepared from the solutions will reflect this property. In this context, we also evaluated the preliminary photovoltaic performance of such films. Planar solar cells were fabricated with an architecture of FTO/TiO_2/perovskite/ spiro-OMeTAD/Au for (mPDA)$MA_{n-1}Pb_nI_{3n+1}$ (n = 1-6) perovskite films. The efficiencies (PCEs) gradually increase from 0.01% to 6.16% with increasing n number from 1 to 6 for (mPDA)$MA_{n-1}Pb_nI_{3n+1}$ (n = 1-6) perovskite devices (**Figure 6d**, Table S2). The negligible photovoltaic outcome of devices with low n values can be attributed to poor surface coverage and the light absorption limitation of the wide band gap n = 1 phase. As the nominal n value increases, there is beneficial generation and dissociation of charges, giving significant increases in the short-circuit current density (J_{sc}) from 1.73 to 14.74 mA cm^{-2}, open-circuit voltage (V_{oc}) from 0.03 to 0.82 V and fill factor (FF) from 0.23 to 0.51. The stability of the

unencapsulated devices examined under ambient conditions environment (20 ºC, humidity of 40 RH%) was improved compared to the unencapsulated films. Devices with nominal n = 6 showed better stability than lower n value, as shown in Figure S9. This can be ascribed to poor film quality for the lower n film, where the large amount of grain boundaries accelerates moisture attack.

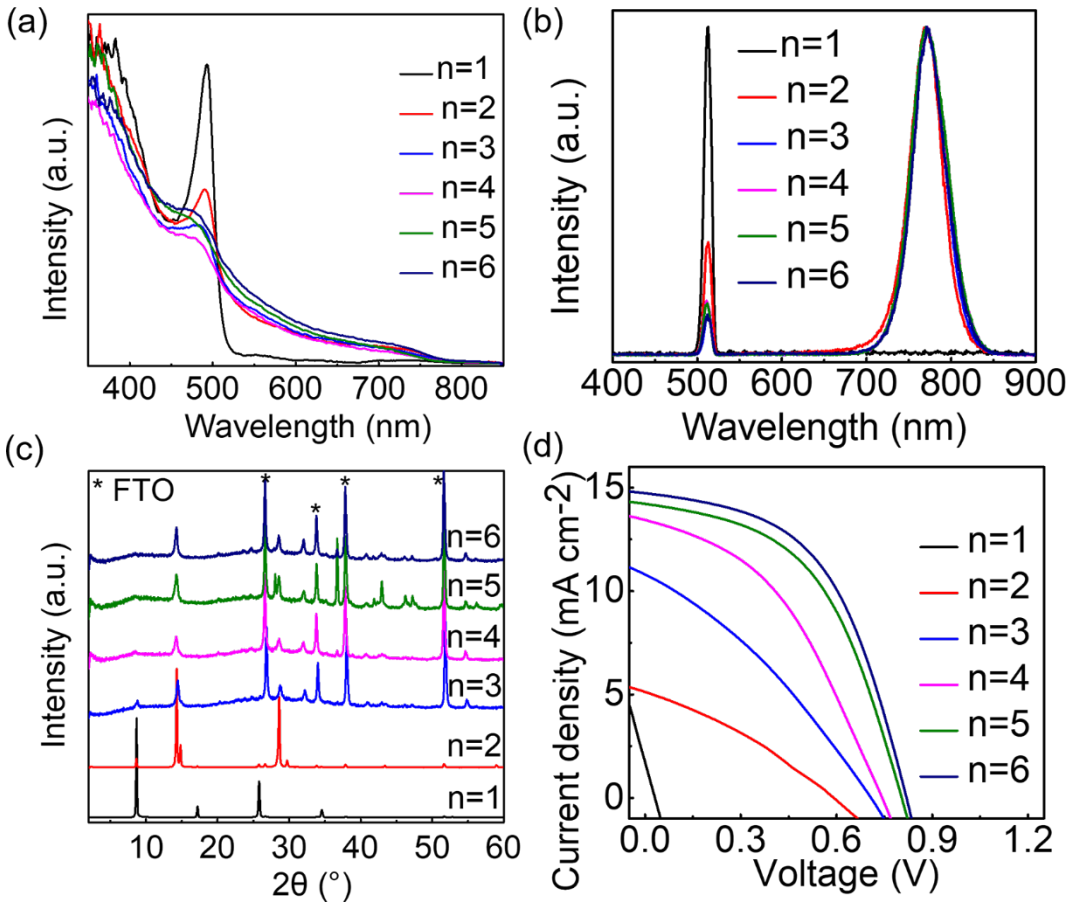

Figure 6. Film properties of (mPDA)$MA_{n-1}Pb_nI_{3n+1}$ (n = 1-6), (a) UV-Vis absorption spectra, (b) steady-state PL spectra, the first peak at 512 nm showing the n =1 phase, the second emission peak at 773 nm showing the 3D bulk phase. (c) PXRD patterns, and (d) *J-V* cures of devices.

Conclusions

We have shown new series of 2D perovskites of (mPDA)$MA_{n-1}Pb_nI_{3n+1}$ (n = 1, 2, and 3) with the DJ type structures. The short aromatic spacer cation of mPDA influences the structure and properties of 2D perovskite. The Pb−I−Pb angles of the (mPDA)$MA_{n-1}Pb_nI_{3n+1}$ (n = 2 and 3) are among the smallest observed because of large octahedral tilting compared with the other 3AMP, 4AMP and BA series. Therefore, the (mPDA)$MA_{n-1}Pb_nI_{3n+1}$ (n = 2 and 3) series show larger band gaps than the other DJ structures. This is despite the fact that they show very close I···I interlayer distances imposed by the compact size of the spacer cation. The analysis suggests that the mPDA-based series have suitable properties for optoelectronic devices. Interestingly, the film growth properties of this class are different from those of the AMP and AMPY based series. Solutions of nominal composition (mPDA)$MA_{n-1}Pb_nI_{3n+1}$ (n = 1-6) give films that are composed of with n = 1 2D and 3D $MAPbI_3$. These results suggest that dissolving the precursors and casting films of nominal compositions cannot guarantee formation of the desired 2D perovskite pure phases. For n > 1, strain accumulation in the perovskite lattice is one of the possible mechanisms to explain why the multilayer 2D phases cannot form in thin films, but a mixture of, 2D n=1 and 3D phases is favored instead. By comparison, multilayer BA-based RP and 4AMP-based DJ phases with reduced internal strain in n>2 phases,[50] can be obtained in the thin films . This indicates the importance of precise structural investigations by single crystal X-ray crystallography to understand the bonding details and interplay between the organic and inorganic components in these hybrid systems. The study also suggests that it is important to investigate many different organic spacer cations in the DJ class of

perovskites to complete the emerging picture of structure-property relationships.

Experimental Section

Materials. Lead oxide (PbO, 99%), methylamine hydrochloride (CH_3NH_3Cl, 99%), hydriodic acid (HI, 57 wt % in H_2O), hypophosphorous acid (H_3PO_2, 50 wt % in H_2O) and m-Phenylenediammonium were used as received from Sigma-Aldrich without further purification. N, N-dimethylformamide (DMF, anhydrous, 99.8%), Dimethyl sulfoxide (DMSO), $TiCl_4$ were purchased from National drug group chemical reagents Co., Ltd., Lead iodide (PbI_2, 99.99%), methylammoium iodide (CH_3NH_3I) were purchased from Xi'an Polymer Light Technology Corp.

Synthesis of $(mPDA)(MA)_{n-1}Pb_nI_{3n+1}$. For n = 1, an amount of 446.4 mg (2 mmol) of 99.9% PbO powder was dissolved in 3 mL of hydrochloric acid and 1 mL of hypophosphorous acid solution by heating under stirring for 5−10 min at ∼200 °C until the solution turned clear. Then 64.9 mg (0.6 mmol) of mPDA were added directly to the above solution under heating and stirring until dissolve totally. White plate-like crystals precipitate of $(mPDA)PbCl_4$ were obtained when cooling to 120 °C. Then the white powder $(mPDA)PbCl_4$ was separated and added into 3 mL of hydroiodic acid and 1 mL of hypophosphorous acid solution and the hot plate was heated at 200 °C until the crystals were dissolved. Then the temperature was cooled to 120 °C, orange plate-like crystals of $(mPDA)PbI_4$ were obtained. The product was isolated by suction filtration followed by drying on the filtration funnel for 30 min. Yield: 368 mg (22.3% based on

total Pb content).

For n = 2, an amount of 446.4 mg (2 mmol) of 99.9% PbO powder was dissolved in 3 mL of hydroiodic acid and 1 mL of hypophosphorous acid solution by heating under stirring for 5-10 min at 200 °C until the solution turned clear bright yellow. The 67.7 mg (1 mmol) of methylammonium chloride (MACl) and 64.9 mg (0.6 mmol) of mPDA were added directly to the above solution under heating and stirring until dissolved totally. Then the temperature was lowered to 120 °C and red plate-like crystals precipitated. The product was isolated by suction filtration followed by drying under vacuum for 30 min. Yield: 418 mg (39.3% based on total Pb content).

For n=3, an amount of 669 mg (3 mmol) of 99.9% PbO powder was dissolved in 5 mL of hydroiodic acid and 1 mL of hypophosphorous acid solution by heating under stirring for 5-10 min at 200 °C until the solution turned clear bright yellow. 135.4 mg (2 mmol) of methylammonium chlorine (MACl) and 77.9 mg (0.6 mmol) of mPDA were added directly to the above solution under heating and stirring until dissolved totally. Then the temperature was cooled to 120 °C, and dark red crystals precipitated. The product was isolated by suction filtration followed by drying on the filtration funnel for 30 min. Yield: 469 mg (36.1% based on total Pb content).

Crystal Materials Characterization. Single-crystal X-ray diffraction experiments were performed using a STOE IPDS II or IPDS 2T diffractometer with Mo Kα radiation (λ = 0.71073 Å) and operating at 50 kV and 40 mA. Integration and numerical absorption corrections were performed using the X-AREA, X-RED, and X-SHAPE

programs. The structures were solved by charge flipping and refined by full-matrix least-squares on F2 using the Jana2006 package. The PLATON software46 was used to identify the twinning domains and validate the space groups of the compounds. Powder X-ray diffraction measurements were carried out on a Rigaku MiniFlex600 X-ray diffractometer (Cu Kα radiation, λ = 1.5406 Å) operating at 40 kV and 15 mA. Optical diffuse reflectance measurements were performed using a Shimadzu UV-3600 UV-vis-NIR spectrometer operating in the 200-1000 nm region using $BaSO_4$ as the reference of 100% reflectance. The band gap of the material was estimated by converting reflectance to absorption according to the Kubelka-Munk equation: $\alpha/S = (1-R)^2(2R)^{-1}$, where R is the reflectance and α and S are the absorption and scattering coefficients, respectively. Steady-state PL spectra were tested by HORIBA LabRAM HR Evolution confocal RAMAN microscope with 473 nm laser.

Solar Cell Device Fabrication. The FTO-coated glass substrates (Pilkington, 15 $\Omega\ sq^{-1}$) were cleaned by ultrasonic bath sequentially with acetone, ethyl alcohol, and deionized water for 15 min respectively, followed by a 15 min UV Ozone treatment. The electronic transport layer of TiO_2 was prepared by chemical bath deposition with the clean substrate immersed in a 0.2 M $TiCl_4$ aqueous solution with the at 70 °C for 1 h. Before the perovskite films preparation, the cleaned FTO/TiO_2 substrates were exposed to ultraviolet light and ozone for 10 min. Precursor solutions were made by mixing $mPDAI_2$, MAI and PbI_2 in stoichiometric ratio with the formula of (mPDA)$MA_{n-1}Pb_nI_{3n+1}$ (n = 1-6). Then an appropriate amount of (mPDA)$MA_{n-1}Pb_nI_{3n+1}$ (n = 3)

precursor solution was dropped on the TiO_2 surface and spin-casted at a low speed of 500 rpm for 3 s followed by a high speed of 4000 rpm for 60 s, and at ca. 45 s before the end of the last spin-coating step, 300 μL of chlorobenzene solvent was dropped onto the substrate. Then films were annealed at 100°C for 10 min. The spiro-MeOTAD solution was prepared by dissolving 72.3 mg of spiro-MeOTAD in 1 ml of chlorobenzene, to which 28.8 μl of 4-tert-butylpyridine and 17.5 μl of lithiumbis(trifluoromethanesulfonyl)imide(Li-TFSI) solution (520 mg LI-TSFI in 1 ml acetonitrile, Sigma-Aldrich, 99.8%) were added. The spiro-MeOTAD solution was spin coated on perovskite films with the speed of 5000 rpm for 30 s. At last, 80 nm Au was evaporated. The active area of the device was 0.09 cm^2.

Thin Film and Solar Cell Device Characterization. SEM images were characterized by SEM (FE-SEM; SU-8020, Hitachi) at an acceleration voltage of 3 kV. UV−visible absorption spectra were acquired on a PerkinElmer UV-Lambda 950 instrument. Steady-state photoluminescence (PL) (excitation at 510 nm, front-side excitation) and time-resolved photoluminescence (TRPL) (excitation at 510 nm, front-side excitation) were measured with a PicoQuant FT-300. Film XRD were carried out in a θ–2θ configuration with a scanning interval of 2θ between 3° and 60° on a Rigaku Smart Lab (X-ray Source: Cu Kα; λ = 1.54 Å). Film TG measurement was conducted by thermoanalyzer systems from 20-500 °C. The *J*−*V* cures were collected in air without any encapsulation using a Keithley 2400 source meter under simulated AM 1.5G irradiation (100 mW/cm^2) generated by a standard solar simulator. The light intensity

was calibrated by using an NREL-certified monocrystalline Si reference cell to reduce the spectral mismatch.

ASSOCIATED CONTENT

Supporting Information

The materials characterization, crystallographic details of (mPDA)$MA_{n-1}Pb_nI_{3n+1}$ (n = 1, 2, 3), computational details, projected density of states, additional results from DFT-1/2 calculations, SEM images and device stability.

X-ray crystallographic data for (mPDA)PbI_4 (CIF).

X-ray crystallographic data for (mPDA)$MAPb_2I_7$ (CIF).

X-ray crystallographic data for (mPDA)$MA_2Pb_3I_{10}$ (CIF).

AUTHOR INFORMATION

Corresponding Authors

m-kanatzidis@northwestern.edu

szliu@dicp.ac.cn

Author Contributions

†These authors contributed equally to this work.

Notes

The authors declare no competing financial interest.

ACKNOWLEDGMENTS

This work was funded by the National Key Research and Development Program of China (2017YFA0204800), the National Natural Science Foundation of China

(62004121), the DNL Cooperation Fund CAS (DNL180311), the 111 Project (B14041) and the Changjiang Scholars and Innovative Research Team (IRT_14R33). At Northwestern University work (synthesis, X-ray diffraction and solar cell fabrication) was supported by ONR grant N00014-20-1-2725. ISCR thanks Dr. S. Tao (Eindhoven University of Technology) for providing the source code of the DFT-1/2 program. B.T. and C.K. acknowledge funding from the European Union's Horizon 2020 program, through an Innovation Action under the grant agreement No. 861985 (PEROCUBE). J.E. acknowledges the financial support from the Institut Universitaire de France. The calculation work was granted access to the HPC resources of [TGCC/CINES/IDRIS] under the allocation 2020-A0080911434 made by GENCI.

REFERENCES

1. Jung, E. H.; Jeon, N. J.; Park, E. Y.; Moon, C. S.; Shin, T. J.; Yang, T. Y.; Noh, J. H.; Seo, J., Efficient, stable and scalable perovskite solar cells using poly(3-hexylthiophene). *Nature* **2019,** *567* (7749), 511-515.
2. Abdollahi Nejand, B.; Hossain, I. M.; Jakoby, M.; Moghadamzadeh, S.; Abzieher, T.; Gharibzadeh, S.; Schwenzer, J. A.; Nazari, P.; Schackmar, F.; Hauschild, D.; Weinhardt, L.; Lemmer, U.; Richards, B. S.; Howard, I. A.; Paetzold, U. W., Vacuum‐Assisted Growth of Low‐Bandgap Thin Films (FA0.8MA0.2Sn0.5Pb0.5I3) for All‐Perovskite Tandem Solar Cells. *Advanced Energy Materials* **2019,** *10* (5), 1902583.
3. Ahlawat, P.; Dar, M. I.; Piaggi, P.; Grätzel, M.; Parrinello, M.; Rothlisberger, U., Atomistic Mechanism of the Nucleation of Methylammonium Lead Iodide Perovskite from Solution. *Chemistry of Materials* **2019,** *32* (1), 529-536.
4. Alsalloum, A. Y.; Turedi, B.; Zheng, X.; Mitra, S.; Zhumekenov, A. A.; Lee, K. J.; Maity, P.; Gereige, I.; AlSaggaf, A.; Roqan, I. S.; Mohammed, O. F.; Bakr, O. M., Low-Temperature Crystallization Enables 21.9% Efficient Single-Crystal MAPbI3 Inverted Perovskite Solar Cells. *ACS Energy Letters* **2020,** *5* (2), 657-662.
5. Barranco, A.; Lopez‐Santos, M. C.; Idigoras, J.; Aparicio, F. J.; Obrero‐Perez, J.; Lopez‐Flores, V.; Contreras‐Bernal, L.; Rico, V.; Ferrer, J.; Espinos, J. P.; Borras, A.; Anta, J. A.; Sanchez‐Valencia, J. R., Enhanced Stability of Perovskite Solar Cells Incorporating Dopant‐Free Crystalline Spiro‐OMeTAD Layers by Vacuum Sublimation. *Advanced Energy Materials* **2019,** *10* (2), 1901524.
6. Liu, Y. C.; Zhang, Y. X.; Zhao, K.; Yang, Z.; Feng, J. S.; Zhang, X.; Wang, K.; Meng, L. N.; Ye, H. C.; Liu, M.; Liu, S. Z., A 1300 mm(2) Ultrahigh-Performance Digital Imaging Assembly using High-Quality Perovskite Single Crystals. *Advanced materials* **2018,** *30* (29).
7. Wei, H. T.; Fang, Y. J.; Mulligan, P.; Chuirazzi, W.; Fang, H. H.; Wang, C. C.; Ecker, B. R.; Gao, Y. L.; Loi, M. A.; Cao, L.; Huang, J. S., Sensitive X-ray detectors made of methylammonium lead tribromide perovskite single crystals. *Nature Photonics* **2016,** *10* (5), 333-+.
8. Shrestha, S.; Fischer, R.; Matt, G. J.; Feldner, P.; Michel, T.; Osvet, A.; Levchuk, I.; Merle, B.; Golkar, S.; Chen, H. W.; Tedde, S. F.; Schmidt, O.; Hock, R.; Ruhrig, M.; Goken, M.; Heiss, W.; Anton, G.; Brabec, C. J., High-performance direct conversion X-ray detectors based on sintered hybrid lead triiodide perovskite wafers. *Nature Photonics* **2017,** *11* (7), 436-+.
9. Stoumpos, C. C.; Malliakas, C. D.; Peters, J. A.; Liu, Z.; Sebastian, M.; Im, J.; Chasapis, T. C.; Wibowo, A. C.; Chung, D. Y.; Freeman, A. J.; Wessels, B. W.; Kanatzidis, M. G., Crystal Growth of the Perovskite Semiconductor $CsPbBr_3$: A New Material for High-Energy Radiation Detection. *Cryst. Growth Des.* **2013,** *13* (7), 2722-2727.

10. He, Y.; Matei, L.; Jung, H. J.; McCall, K. M.; Chen, M.; Stoumpos, C. C.; Liu, Z.; Peters, J. A.; Chung, D. Y.; Wessels, B. W.; Wasielewski, M. R.; Dravid, V. P.; Burger, A.; Kanatzidis, M. G., High spectral resolution of gamma-rays at room temperature by perovskite CsPbBr3 single crystals. *Nature Communications* **2018,** *9*.
11. Han, B. N.; Yuan, S. C.; Fang, T.; Zhang, F. J.; Shi, Z. F.; Song, J. Z., Novel Lewis Base Cyclam Self-Passivation of Perovskites without an Anti-Solvent Process for Efficient Light-Emitting Diodes. *ACS applied materials & interfaces* **2020,** *12* (12), 14224-14232.
12. Lee, C. C.; Chen, C. I.; Fang, C. T.; Huang, P. Y.; Wu, Y. T.; Chueh, C. C., Improving Performance of Perovskite Solar Cells Using [7]Helicenes with Stable Partial Biradical Characters as the Hole‐Extraction Layers. *Adv. Funct. Mater.* **2019,** *29* (13), 1808625.
13. Du, H. Y.; Hui, W.; Tang, L. Q.; Qiu, J.; Niu, T. T.; Yang, Y. G.; Gao, X. Y.; Xia, Y. D.; Chen, Y. H.; Huang, W., Highly oriented perovskites for efficient light-emitting diodes with balanced charge transport. *Organic Electronics* **2020,** *77*.
14. Tsai, H.; Liu, C. M.; Kinigstein, E.; Li, M. X.; Tretiak, S.; Cotlet, M.; Ma, X. D.; Zhang, X. Y.; Nie, W. Y., Critical Role of Organic Spacers for Bright 2D Layered Perovskites Light-Emitting Diodes. *Advanced science* **2020,** *7* (7).
15. Zeng, S. Y.; Shi, S. S.; Wang, S. R.; Xiao, Y., Mixed-ligand engineering of quasi-2D perovskites for efficient sky-blue light-emitting diodes. *Journal of Materials Chemistry C* **2020,** *8* (4), 1319-1325.
16. Mei, A. Y.; Li, X.; Liu, L. F.; Ku, Z. L.; Liu, T. F.; Rong, Y. G.; Xu, M.; Hu, M.; Chen, J. Z.; Yang, Y.; Gratzel, M.; Han, H. W., A hole-conductor-free, fully printable mesoscopic perovskite solar cell with high stability. *Science* **2014,** *345* (6194), 295-298.
17. Blancon, J.-C.; Even, J.; Stoumpos, C. C.; Kanatzidis, M. G.; Mohite, A. D., Semiconductor physics of organic-inorganic 2D halide perovskites. *Nature Nanotechnology* **2020,** *15* (12), 969-985.
18. Stranks, S. D.; Eperon, G. E.; Grancini, G.; Menelaou, C.; Alcocer, M. J. P.; Leijtens, T.; Herz, L. M.; Petrozza, A.; Snaith, H. J., Electron-Hole Diffusion Lengths Exceeding 1 Micrometer in an Organometal Trihalide Perovskite Absorber. *Science* **2013,** *342* (6156), 341-344.
19. Yang, W. S.; Park, B.-W.; Jung, E. H.; Jeon, N. J.; Kim, Y. C.; Lee, D. U.; Shin, S. S.; Seo, J.; Kim, E. K.; Noh, J. H.; Seok, S. I., Iodide management in formamidinium-lead-halide-based perovskite layers for efficient solar cells. *Science* **2017,** *356* (6345), 1376-+.
20. Si, H.; Zhang, Z.; Liao, Q.; Zhang, G.; Ou, Y.; Zhang, S.; Wu, H.; Wu, J.; Kang, Z.; Zhang, Y., A-Site Management for Highly Crystalline Perovskites. *Adv. Mater.* **2020,** *32* (4).

21. Wang, S.; Jiang, Y.; Juarez-Perez, E. J.; Ono, L. K.; Qi, Y., Accelerated degradation of methylammonium lead iodide perovskites induced by exposure to iodine vapour. *Nature Energy* **2017,** *2* (1).
22. Yoo, J. J.; Seo, G.; Chua, M. R.; Park, T. G.; Lu, Y.; Rotermund, F.; Kim, Y.-K.; Moon, C. S.; Jeon, N. J.; Correa-Baena, J.-P.; Bulović, V.; Shin, S. S.; Bawendi, M. G.; Seo, J., Efficient perovskite solar cells via improved carrier management. *Nature* **2021,** *590* (7847), 587-593.
23. Mao, L.; Stoumpos, C. C.; Kanatzidis, M. G., Two-Dimensional Hybrid Halide Perovskites: Principles and Promises. *Journal of the American Chemical Society* **2019,** *141* (3), 1171-1190.
24. Li, X.; Hoffman, J. M.; Kanatzidis, M. G., The 2D Halide Perovskite Rulebook: How the Spacer Influences Everything from the Structure to Optoelectronic Device Efficiency. *Chem. Rev.* **2021,** *121* (4), 2230-2291.
25. Li, X. T.; Guo, P. J.; Kepenekian, M.; Hadar, I.; Katan, C.; Even, J.; Stoumpos, C. C.; Schaller, R. D.; Kanatzidis, M. G., Small Cyclic Diammonium Cation Templated (110)-Oriented 2D Halide (X = I, Br, Cl) Perovskites with White-Light Emission. *Chemistry of Materials* **2019,** *31* (9), 3582-3590.
26. Li, X. T.; Ke, W. J.; Traore, B.; Guo, P. J.; Hadar, I.; Kepenekian, M.; Even, J.; Katan, C.; Stoumpos, C. C.; Schaller, R. D.; Kanatzidis, M. G., Two-Dimensional Dion-Jacobson Hybrid Lead Iodide Perovskites with Aromatic Diammonium Cations. *Journal of the American Chemical Society* **2019,** *141* (32), 12880-12890.
27. Chen, Y.; Sun, Y.; Peng, J.; Tang, J.; Zheng, K.; Liang, Z., 2D Ruddlesden-Popper Perovskites for Optoelectronics. *Adv. Mater.* **2018,** *30* (2).
28. Stoumpos, C. C.; Cao, D. H.; Clark, D. J.; Young, J.; Rondinelli, J. M.; Jang, J. I.; Hupp, J. T.; Kanatzidis, M. G., Ruddlesden-Popper Hybrid Lead Iodide Perovskite 2D Homologous Semiconductors. *Chemistry of Materials* **2016,** *28* (8), 2852-2867.
29. Mao, L.; Ke, W.; Pedesseau, L.; Wu, Y.; Katan, C.; Even, J.; Wasielewski, M. R.; Stoumpos, C. C.; Kanatzidis, M. G., Hybrid Dion-Jacobson 2D Lead Iodide Perovskites. *J. Am. Chem. Soc.* **2018,** *140* (10), 3775-3783.
30. Soe, C. M. M.; Stoumpos, C. C.; Kepenekian, M.; Traore, B.; Tsai, H.; Nie, W.; Wang, B.; Katan, C.; Seshadri, R.; Mohite, A. D.; Eyen, J.; Marks, T. J.; Kanatzidis, M. G., New Type of 2D Perovskites with Alternating Cations in the Interlayer Space, (C(NH2)(3))(CH3NH3)(n)PbnI3n+1: Structure, Properties, and Photovoltaic Performance. *J. Am. Chem. Soc.* **2017,** *139* (45), 16297-16309.
31. Ke, W.; Mao, L.; Stoumpos, C. C.; Hoffman, J.; Spanopoulos, I.; Mohite, A. D.; Kanatzidis, M. G., Compositional and Solvent Engineering in Dion-Jacobson 2D Perovskites Boosts Solar Cell Efficiency and Stability. *Advanced Energy Materials* **2019,** *9* (10), 1803384.

32. Jung, H. J.; Stompus, C. C.; Kanatzidis, M. G.; Dravid, V. P., Self-Passivation of 2D Ruddlesden-Popper Perovskite by Polytypic Surface PbI2 Encapsulation. *Nano letters* **2019,** *19* (9), 6109-6117.
33. Jodlowski, A. D.; Roldán-Carmona, C.; Grancini, G.; Salado, M.; Ralaiarisoa, M.; Ahmad, S.; Koch, N.; Camacho, L.; de Miguel, G.; Nazeeruddin, M. K., Large guanidinium cation mixed with methylammonium in lead iodide perovskites for 19% efficient solar cells. *Nature Energy* **2017,** *2* (12), 972-979.
34. Hoffman, J. M.; Che, X.; Sidhik, S.; Li, X.; Hadar, I.; Blancon, J. C.; Yamaguchi, H.; Kepenekian, M.; Katan, C.; Even, J.; Stoumpos, C. C.; Mohite, A. D.; Kanatzidis, M. G., From 2D to 1D Electronic Dimensionality in Halide Perovskites with Stepped and Flat Layers Using Propylammonium as a Spacer. *Journal of the American Chemical Society* **2019,** *141* (27), 10661-10676.
35. Cho, Y.; Soufiani, A. M.; Yun, J. S.; Kim, J.; Lee, D. S.; Seidel, J.; Deng, X.; Green, M. A.; Huang, S.; Ho-Baillie, A. W. Y., Mixed 3D-2D Passivation Treatment for Mixed-Cation Lead Mixed-Halide Perovskite Solar Cells for Higher Efficiency and Better Stability. *Advanced Energy Materials* **2018,** *8* (20), 1703392.
36. Li, X. T.; Hoffman, J.; Ke, W. J.; Chen, M.; Tsai, H.; Nie, W. Y.; Mohite, A. D.; Kepenekian, M.; Katan, C.; Even, J.; Wasielewski, M. R.; Stoumpos, C. C.; Kanatzidis, M. G., Two-Dimensional Halide Perovskites Incorporating Straight Chain Symmetric Diammonium Ions, (NH3CmH2mNH3)(CH3NH3)(n-1)PbnI3n+1 (m=4-9; n=1-4). *Journal of the American Chemical Society* **2018,** *140* (38), 12226-12238.
37. Shen, Y.; Liu, Y.; Ye, H.; Zheng, Y.; Wei, Q.; Xia, Y.; Chen, Y.; Zhao, K.; Huang, W.; Liu, S., Centimeter-Sized Single Crystal of Two-Dimensional Halide Perovskites Incorporating Straight-Chain Symmetric Diammonium Ion for X-Ray Detection. *Angewandte Chemie-International Edition* **2020,** *59* (35), 14896-14902.
38. Xu, Z.; Mitzi, D. B.; Medeiros, D. R., [(CH3)3NCH2CH2NH3]SnI4: A Layered Perovskite with Quaternary/Primary Ammonium Dications and Short Interlayer Iodine−Iodine Contacts. *Inorg. Chem.* **2003,** *42* (5), 1400-1402.
39. Li, X.; Ke, W.; Traoré, B.; Guo, P.; Hadar, I.; Kepenekian, M.; Even, J.; Katan, C.; Stoumpos, C. C.; Schaller, R. D.; Kanatzidis, M. G., Two-Dimensional Dion–Jacobson Hybrid Lead Iodide Perovskites with Aromatic Diammonium Cations. *J. Am. Chem. Soc.* **2019,** *141* (32), 12880-12890.
40. Li, Y.; Milic, J. V.; Ummadisingu, A.; Seo, J. Y.; Im, J. H.; Kim, H. S.; Liu, Y. H.; Dar, M. I.; Zakeeruddin, S. M.; Wang, P.; Hagfeldt, A.; Gratzel, M., Bifunctional Organic Spacers for Formamidinium-Based Hybrid Dion-Jacobson Two-Dimensional Perovskite Solar Cells. *Nano letters* **2019,** *19* (1), 150-157.
41. Lemmerer, A.; Billing, D. G., Two packing motifs based upon chains of edge-sharing PbI6 octahedra. *Acta crystallographica. Section C, Crystal structure communications* **2006,** *62* (Pt 12), m597-601.

42. Dobrzycki, L.; Wozniak, K., Inorganic-organic hybrid salts of diaminobenzenes and related cations. *Crystengcomm* **2008,** *10* (5), 577-589.
43. Zhang, F.; Lu, H.; Tong, J.; Berry, J. J.; Beard, M. C.; Zhu, K., Advances in two-dimensional organic–inorganic hybrid perovskites. *Energy Environ. Sci.* **2020,** *13* (4), 1154-1186.
44. Huang, P.; Kazim, S.; Wang, M.; Ahmad, S., Toward Phase Stability: Dion–Jacobson Layered Perovskite for Solar Cells. *ACS Energy Lett.* **2019,** *4* (12), 2960-2974.
45. Ma, C.; Shen, D.; Ng, T.-W.; Lo, M.-F.; Lee, C.-S., 2D Perovskites with Short Interlayer Distance for High-Performance Solar Cell Application. *Adv. Mater.* **2018,** *30* (22), 1800710.
46. Li, X.; Hoffman, J.; Ke, W.; Chen, M.; Tsai, H.; Nie, W.; Mohite, A. D.; Kepenekian, M.; Katan, C.; Even, J.; Wasielewski, M. R.; Stoumpos, C. C.; Kanatzidis, M. G., Two-Dimensional Halide Perovskites Incorporating Straight Chain Symmetric Diammonium Ions, (NH3CmH2mNH3)(CH3NH3)n−1PbnI3n+1 (m = 4–9; n = 1–4). *J. Am. Chem. Soc.* **2018,** *140* (38), 12226-12238.
47. Li, X.; He, Y.; Kepenekian, M.; Guo, P.; Ke, W.; Even, J.; Katan, C.; Stoumpos, C. C.; Schaller, R. D.; Kanatzidis, M. G., Three-Dimensional Lead Iodide Perovskitoid Hybrids with High X-ray Photoresponse. *J. Am. Chem. Soc.* **2020,** *142* (14), 6625-6637.
48. Li, X.; Fu, Y.; Pedesseau, L.; Guo, P.; Cuthriell, S.; Hadar, I.; Even, J.; Katan, C.; Stoumpos, C. C.; Schaller, R. D.; Harel, E.; Kanatzidis, M. G., Negative Pressure Engineering with Large Cage Cations in 2D Halide Perovskites Causes Lattice Softening. *J. Am. Chem. Soc.* **2020,** *142* (26), 11486-11496.
49. Hoffman, J. M.; Che, X.; Sidhik, S.; Li, X.; Hadar, I.; Blancon, J.-C.; Yamaguchi, H.; Kepenekian, M.; Katan, C.; Even, J.; Stoumpos, C. C.; Mohite, A. D.; Kanatzidis, M. G., From 2D to 1D Electronic Dimensionality in Halide Perovskites with Stepped and Flat Layers Using Propylammonium as a Spacer. *J. Am. Chem. Soc.* **2019,** *141* (27), 10661-10676.
50. Kepenekian, M.; Traore, B.; Blancon, J.-C.; Pedesseau, L.; Tsai, H.; Nie, W.; Stoumpos, C. C.; Kanatzidis, M. G.; Even, J.; Mohite, A. D.; Tretiak, S.; Katan, C., Concept of Lattice Mismatch and Emergence of Surface States in Two-dimensional Hybrid Perovskite Quantum Wells. *Nano Lett.* **2018,** *18* (9), 5603-5609.
51. Marchenko, E. I.; Korolev, V. V.; Mitrofanov, A.; Fateev, S. A.; Goodilin, E. A.; Tarasov, A. B., Layer Shift Factor in Layered Hybrid Perovskites: Univocal Quantitative Descriptor of Composition–Structure–Property Relationships. *Chem. Mater.* **2021**.
52. Du, K. Z.; Tu, Q.; Zhang, X.; Han, Q. W.; Liu, J.; Zauscher, S.; Mitzi, D. B., Two-Dimensional Lead(II) Halide-Based Hybrid Perovskites Templated by Acene Alkylamines: Crystal Structures, Optical Properties, and Piezoelectricity. *Inorganic chemistry* **2017,** *56* (15), 9291-9302.

53. Li, X.; Hoffman, J.; Ke, W.; Chen, M.; Tsai, H.; Nie, W.; Mohite, A. D.; Kepenekian, M.; Katan, C.; Even, J.; Wasielewski, M. R.; Stoumpos, C. C.; Kanatzidis, M. G., Two-Dimensional Halide Perovskites Incorporating Straight Chain Symmetric Diammonium Ions, (NH3C mH2 mNH3)(CH3NH3) n-1Pb nI3 n+1 (m = 4-9; n = 1-4). *J. Am. Chem. Soc.* **2018,** *140* (38), 12226-12238.
54. Li, X.; Ke, W.; Traore, B.; Guo, P.; Hadar, I.; Kepenekian, M.; Even, J.; Katan, C.; Stoumpos, C. C.; Schaller, R. D.; Kanatzidis, M. G., Two-Dimensional Dion-Jacobson Hybrid Lead Iodide Perovskites with Aromatic Diammonium Cations. *J. Am. Chem. Soc.* **2019,** *141* (32), 12880-12890.
55. Vasileiadou, E. S.; Wang, B.; Spanopoulos, I.; Hadar, I.; Navrotsky, A.; Kanatzidis, M. G., Insight on the Stability of Thick Layers in 2D Ruddlesden–Popper and Dion–Jacobson Lead Iodide Perovskites. *J. Am. Chem. Soc.* **2021,** *143* (6), 2523-2536.
56. Pedesseau, L.; Sapori, D.; Traore, B.; Robles, R.; Fang, H.-H.; Loi, M. A.; Tsai, H.; Nie, W.; Blancon, J.-C.; Neukirch, A.; Tretiak, S.; Mohite, A. D.; Katan, C.; Even, J.; Kepenekian, M., Advances and Promises of Layered Halide Hybrid Perovskite Semiconductors. *Acs Nano* **2016,** *10* (11), 9776-9786.
57. Stoumpos, C. C.; Kanatzidis, M. G., Halide Perovskites: Poor Man's High-Performance Semiconductors. *Adv. Mater.* **2016,** *28* (28), 5778-5793.
58. Perdew, J. P.; Burke, K.; Ernzerhof, M., Generalized Gradient Approximation Made Simple. *Phys. Rev. Lett.* **1996,** *77* (18), 3865-3868.
59. Zhang, Y.; Yang, W., Comment on ``Generalized Gradient Approximation Made Simple". *Phys. Rev. Lett.* **1998,** *80* (4), 890-890.
60. Cuadrado, R.; Pruneda, M.; García, A.; Ordejón, P., Implementation of non-collinear spin-constrained DFT calculations in SIESTA with a fully relativistic Hamiltonian. *J. Phys. Mater.* **2018,** *1* (1), 015010.
61. Ferreira, L. G.; Marques, M.; Teles, L. K., Approximation to density functional theory for the calculation of band gaps of semiconductors. *Phys. Rev. B* **2008,** *78* (12), 125116.
62. Tao, S. X.; Cao, X.; Bobbert, P. A., Accurate and efficient band gap predictions of metal halide perovskites using the DFT-1/2 method: GW accuracy with DFT expense. *Sci. Rep.* **2017,** *7* (1), 14386.
63. Mitzi, D. B., Synthesis, Crystal Structure, and Optical and Thermal Properties of (C4H9NH3)2MI4 (M = Ge, Sn, Pb). *Chem. Mater.* **1996,** *8* (3), 791-800.
64. Dang, Y.; Liu, Y.; Sun, Y.; Yuan, D.; Liu, X.; Lu, W.; Liu, G.; Xia, H.; Tao, X., Bulk crystal growth of hybrid perovskite material CH3NH3PbI3. *Crystengcomm* **2015,** *17* (3), 665-670.

Table 1. Crystal and Refinement Data for $(mPDA)(MA)_{n-1}Pb_nI_{3n+1}$ (n = 1−3).

	$(mPDA)PbI_4$	$(mPDA)(MA)Pb_2I_7$	$(mPDA)(MA)_2Pb_3I_{10}$
Crystal system	monoclinic	monoclinic	orthorhombic
Space group	*Cc*	*Cc*	$Pmc2_1$
Unit cell dimensions	a = 21.727(3) Å b = 9.3607(8) Å c = 7.9858(11) Å β = 105.885(10)°	a = 34.682(3) Å b = 8.8518(9) Å c = 8.7227(7) Å β = 104.491(6)°	a = 23.118(5) Å b = 8.8462(18) Å c = 8.7530(18) Å
Volume	1562.1(3) $Å^3$	2592.6(4) $Å^3$	1790.0(6) $Å^3$
Z	4	4	2
Density (calculated)	3.5078 g/cm^3	3.7018 g/cm^3	3.8273 g/cm^3
Index ranges	-27<=h<=29 -12<=k<=12 -10<=l<=10	-47<=h<=47 -12<=k<=12 -11<=l<=10	-30<=h<=31 -12<=k<=12 -12<=l<=11
Independent reflections	2948 [R_{int} = 0.1]	4480 [R_{int} = 0.0648]	3110 [R_{int} = 0.0611]
Completeness to θ = 25°	100%	99%	97%
Data / restraints / parameters	2948 / 18 / 75	4480 / 15 / 115	3110 / 8 / 86
Goodness-of-fit	3.81	4.12	1.53
Final R indices [I>2σ(I)]	R_{obs} = 0.1221 wR_{obs} = 0.1357	R_{obs} = 0.0487 wR_{obs} = 0.0728	R_{obs} = 0.0353 wR_{obs} = 0.0306
R indices [all data]	R_{all} = 0.1692 wR_{all} = 0.1388	R_{all} = 0.0666 wR_{all} = 0.0739	R_{all} = 0.0448 wR_{all} = 0.0314
Largest diff. peak and hole	12.54 and -6.40 $e·Å^{-3}$	1.81 and -2.99 $e·Å^{-3}$	0.85 and -0.77 $e·Å^{-3}$

Table 2. Summary of Pb-I-Pb Bond Angles.

$(mPDA)PbI_4$		$(mPDA)(MA)Pb_2I_7$		$(mPDA)(MA)_2Pb_3I_{10}$	
Label	Angles (°)	Label	Angles (°)	Label	Angles (°)
Pb(1)-I(4)-Pb(1)#11	144.4(2)	Pb(1)-I(1)-Pb(1)#10	152.96(17)	Pb(1)-I(1)-Pb(1)#8	155.47(8)
Pb(1)-I(5)-Pb(1)#7	143.2(3)	Pb(1)-I(2)-Pb(1)#4	152.51(16)	Pb(1)-I(2)-Pb(1)#9	157.72(7)
		Pb(2)-I(3)-Pb(2)#4	152.18(15)	Pb(2)-I(3)-Pb(2)#10	153.74(5)
		Pb(2)-I(4)-Pb(2)#10	151.93(16)	Pb(2)-I(4)-Pb(2)#11	153.15(5)
		Pb(1)-I(6)-Pb(2)	179.85(17)	Pb(1)-I(5)-Pb(2)	179.24(13)
Axial Pb-I-Pb (°)	-		179.9		179.2
Ave equatorial Pb-I-Pb (°)	143.7		152.4		155.0
Ave Pb-I-Pb (°)	143.7		157.9		159.9

Table 3. Summary of Pb-I Bond Lengths.

$(mPDA)PbI_4$		$(mPDA)(MA)Pb_2I_7$		$(mPDA)(MA)_2Pb_3I_{10}$	
Label	Distances (Å)	Label	Distances (Å)	Label	Distances (Å)
Pb(1)-I(1)#1	3.195(7)	Pb(1)-I(1)	3.202(5)	Pb(1)-I(1)	3.172(3)
Pb(1)-I(2)	3.197(7)	Pb(1)-I(1)#1	3.198(5)	Pb(1)-I(1)#1	3.166(2)
Pb(1)-I(4)	3.251(9)	Pb(1)-I(2)	3.180(5)	Pb(1)-I(2)	3.190(2)
Pb(1)-I(4)#2	3.230(8)	Pb(1)-I(2)#2	3.208(5)	Pb(1)-I(2)#2	3.181(3)
Pb(1)-I(5)	3.235(9)	Pb(1)-I(5)	3.059(5)	Pb(1)-I(5)	3.1932(16)
Pb(1)-I(5)#3	3.229(9)	Pb(1)-I(6)	3.320(7)	Pb(1)-I(5)#3	3.1932(16)
		Pb(2)-I(3)	3.194(5)	Pb(2)-I(3)	3.187(2)
		Pb(2)-I(3)#2	3.213(5)	Pb(2)-I(3)#4	3.2311(17)
		Pb(2)-I(4)	3.196(5)	Pb(2)-I(4)	3.1658(17)
		Pb(2)-I(4)#1	3.204(4)	Pb(2)-I(4)#5	3.203(2)
		Pb(2)-I(6)	3.242(7)	Pb(2)-I(5)	3.2991(17)
		Pb(2)-I(7)	3.129(4)	Pb(2)-I(6)	3.0869(16)

Table 4 Summary of the lattice mismatch.

		mPDA	3AMP[29]	4AMP[29]	BA[28, 63]
n=1	Pb_1-$^{63}Pb_3$	9.361	9.213	9.170 / 8.881	8.863
	Pb_1-Pb_5	7.986	8.673	8.559 / 8.858	8.682
	mismatch[50, 64]	-2.5%	+0.5%	-0.3%	-1.3%
	anisotropy	14%	6%	7%	2%
n=2	Pb_1-Pb_3	8.852	8.861	8.844	8.947
	Pb_1-Pb_5	8.723	8.858	8.841	8.859
	mismatch	-1.2%	-0.4%	-0.6%	+0.7%
	anisotropy	1.4%	0.0%	0.0%	1.0%
n=3	Pb_1-Pb_3	8.846	8.862	8.836	8.927
	Pb_1-Pb_5	8.753	8.862	8.835	8.878
	mismatch	-1.1%	-0.4%	-0.7%	+0.1%
	anisotropy	1.1%	0.0%	0.0%	0.6%

Table 5. Summary of the electronic band structure calculations with revPBE.

Cation		Band gap (eV)	Band dispersion [a] (meV)		Effective mass (m_0) [b]		
			VBM	CBM	m_h	m_e	μ
mPDA	n=2	0.92	63	27	0.26	0.20	0.11
	n=3	0.86	67	79	0.19	0.17	0.09
BA	n = 2	0.93	1	<1	0.21	0.14	0.085
	n = 3	0.70	1	1	0.14	0.12	0.066
4AMP	n=2	0.66	53	25	0.22	0.18	0.10
	n=3	0.69	87	45	0.18	0.16	0.08
3AMP	n=2	0.44	43	32	0.15	0.13	0.07
	n=3	0.35	70	46	0.18	0.14	0.08

a. Band dispersion in the stacking direction
b. Average effective mass in the in-plane direction

TOC Graphic